Türkiye Jeoloji Bülteni
Geological Bulletin of Turkey
69 (2026) 183-202
doi: 10.25288/tjb.1807185

Remote Sensing of Listvenite Hydrothermal Alteration in Vezirler Mélange, Kula (Western Türkiye): Landsat-7 ETM+, Crosta-PCA and Band-Ratio Mapping

Kula (Batı Türkiye) Vezirler Karmaşığındaki Listvenitik Hidrotermal Alterasyonunun Uzaktan Algılanması: Landsat-7 ETM+, Crosta-PCA ve Bant-Oranı Haritalaması

Semih Eski[1, *], Mehmet Akbulut[1]

[1] *Dokuz Eylül University, Faculty of Engineering, Department of Geological Engineering, Central Campus, 35390 İzmir, Türkiye*

• Geliş/Received: 20.10.2025 • Düzeltilmiş Metin Geliş/Revised Manuscript Received: 29.12.2025 • Kabul/Accepted: 01.01.2026
• Çevrimiçi Yayın/Available online: 22.02.2026 • Baskı/Printed: 30.04.2026

Araştırma Makalesi/Research Article *Türkiye Jeol. Bül. / Geol. Bull. Turkey*

Abstract: Listvenite-type silica–carbonate metasomatic alteration in the Vezirler ophiolitic mélange (northeastern Kula, western Türkiye) was screened using a lithology-masked Selective PCA workflow and complementary band-ratio indices applied to a cloud-free Landsat-7 ETM+ image. Masking reduced spectral mixing from vegetation, alluvium, and non-target lithologies and increased anomaly contrast within a field-verified ROI. Ferric-iron–sensitive PC2 anomalies cluster along carbonatized/silicified serpentinites (CS-Srp) and Fe-oxide-stained silica–carbonate caps (Fscc/Cnz), consistent with hematite coatings documented in the field. Ferrous-iron responses are comparatively subdued, indicating limited preservation of surface-expressed Fe^{2+} signatures under pervasive oxidation and overprinting. Hydroxyl-related patterns delineate alteration halos but weaken over strongly silicified caps where diagnostic OH absorption is suppressed. Band-ratio maps (Fe^{3+}: B3/B2; silica: B7/B5; OH^{-}: B5/(B5 + B7)), statistically segmented using $\mu \pm \sigma$ thresholds, reproduce first-order PCA patterns and support repeatable anomaly ranking. The results demonstrate a rapid regional screening approach relevant to alteration targeting and natural mineral carbonation analogues, while recognizing inherent limitations of the 30 m resolution, such as false positives in shaded valleys due to topographic effects and spectral dilution from mixed-pixel responses along slope transitions. Future work may integrate ASTER TIR and archival ASTER SWIR scenes acquired prior to 2008, or modern SWIR/hyperspectral datasets, to improve mineral discrimination.

Keywords: Band ratios, Crosta-PCA, iron oxides, Kula, Landsat-7 ETM+, listvenite, silica-carbonate alteration, remote sensing.

Öz: *Vezirler ofiyolitik melanjı (Kula'nın kuzeydoğusu, Batı Türkiye) içerisindeki listvenit tipi silis–karbonat metasomatik alterasyon, litoloji/ROI maskelemesi uygulanmış Seçimli PCA (Selective PCA) iş akışı ve tamamlayıcı bant-oranı indeksleri ile bulut içermeyen bir Landsat-7 ETM+ görüntüsü üzerinden taranmıştır. Maskeleme, bitki örtüsü, alüvyon ve hedef dışı litolojilerden kaynaklanan spektral karışımı azaltarak saha ile doğrulanmış ROI içinde anomali kontrastını artırmıştır. Ferrik demire duyarlı PC2 anomalileri, karbonatlaşmış/silisleşmiş serpantinitler (CS-Srp) ile Fe-oksit boyalı silis–karbonat şapkalar (Fscc/Cnz) boyunca kümelenmekte ve arazide gözlenen hematitleşmiş kaplamalarla uyum göstermektedir.* Fe^{2+} *tepkileri daha zayıftır ve yüzeyde ileri oksidasyon/overprinting koşullarında* Fe^{2+} *imzalarının sınırlı korunduğunu düşündürmektedir. Hidroksil ile ilişkili desenler alterasyon halelerini işaret etse de kuvvetli silisleşmiş şapkalarda OH soğurmalarının baskılanması nedeniyle zayıflayabilmektedir. Bant-oranı haritaları (*Fe^{3+}*: B3/B2; silis: B7/B5;* OH^{-}*: B5/(B5+B7)) ve* $\mu \pm \sigma$ *ile istatistiksel sınıflama, PCA desenlerini doğrulayarak tekrarlanabilir hedef sıralaması sağlamıştır. Sonuçlar, gölgeli vadilerde*

---

[*] Correspondence / *Yazışma*: semih.eski@deu.edu.tr

http://tjb.jmo.org.tr
http://dergipark.gov.tr/tjb

topoğrafya kaynaklı sahte anomaliler ve eğim geçişlerinde piksel-içi karışım nedeniyle oluşan spektral seyrelme gibi 30 m çözünürlüğe özgü sınırlılıkları dikkate alarak, bölgesel ölçekte hızlı alterasyon taramasını mümkün kılmaktadır. Gelecek çalışmalarda ASTER TIR ve 2008 öncesi arşiv ASTER SWIR sahneleri veya modern SWIR/hiperspektral veriler ile mineral ayrımı güçlendirilebilir.

Anahtar Kelimeler: *Bant oranları, Crosta-PCA, demir oksit, Kula, Landsat-7 ETM+, listvenit, karbonat alterasyonu, uzaktan algılama.*

INTRODUCTION

Remote sensing techniques have become essential tools for mineral exploration, particularly for the rapid identification of economically significant mineralization in large and often inaccessible terrain. One of the pioneering demonstrations of this potential was presented by Abrams et al. (1983), who successfully delineated porphyry copper-related alteration zones in southern Arizona using multispectral Landsat data. Subsequent studies have advanced these capabilities through refined image processing techniques and sensor improvements. For instance, Crosta and Moore (1989) significantly enhanced mineral detection capabilities by identifying specific eigenvector combinations in Thematic Mapper imagery that isolate ferric-iron and hydroxyl-bearing clay minerals, underscoring the importance of tailored principal components analysis (PCA) configurations for different geological settings.

The launch of Landsat 7 ETM+ in 1999 introduced shortwave infrared (SWIR) spectral bands particularly sensitive to distinguishing iron oxide and clay alteration minerals, enabling high-resolution mineralogical mapping at regional scale (Segal, 1982; Aydal et al., 2007; Khaleghi et al. 2020). Numerous studies have demonstrated that basaltic volcanic fields undergo intense chemical weathering of young basaltic lavas and tuffs, leading to the formation of iron oxide minerals, primarily hematite (α-Fe_2O_3), goethite (α-FeOOH), and limonite ($FeO(OH)\cdot nH_2O$) in surface or near-surface horizons. Deeper profiles often exhibit alteration of volcanic glass into clay minerals, notably smectite, illite, and kaolinite, which significantly influence soil properties by enhancing water retention and swelling, directly impacting local erosion and agricultural productivity (Colman, 1982; Bishop et al., 1998; Gomboš, 2012; Silva et al., 2020). Such assessments from remote sensing imagery are also critical for mineral exploration campaigns, for remotely locating the main iron (and occasionally transitional metal) oxide +/- silica-rich zones, namely the gossans. Gossan zones occur through leaching of the buried sub-surface sulfide mineralization, due to the effects of oxidizing surficial and/or near-surface processes, and are considered as useful marker buoys for detecting a potential economic mineralization.

Extensive iron oxide-bearing weathering profiles and/or occurrence of gossan-like ferruginous and silica-carbonate alteration zones (listvenite – *sensu lato*) are also very significant for mantle rocks of the ophiolitic series. Mapping of the listvenite bodies is particularly important due to their potential for precious metal mineralization. Besides their potential economic importance listvenites also play another role in the current search for remedies to the global climate crisis. These occurrences are natural analogues of mineral carbonation that is being considered as a way of reducing atmospheric CO_2 levels, and lately they are being studied in this respect (Akbulut et al., 2024 and references therein). For this, introduction of CO_2-bearing low-temperature hydrothermal fluids into a serpentinized peridotite host is essential.

The Kula region, situated at the western termination of Türkiye’s east-west trending northern ophiolitic belt (Figure 1), benefits from a unique geological setting hosting notable hot springs and well-preserved remnants of the Tethyan oceanic lithosphere. Located within the Kula-Salihli UNESCO Global Geopark, the area has been the subject of extensive geological investigations (e.g., Ercan, 1981; Ercan et al., 1992; Şen, 2002; Binal and Ercanoğlu, 2010; Aytaç and Demir, 2023; Akbulut et al., 2024). Despite this rich geological understanding, systematic remote sensing-based mineral mapping efforts remain limited.

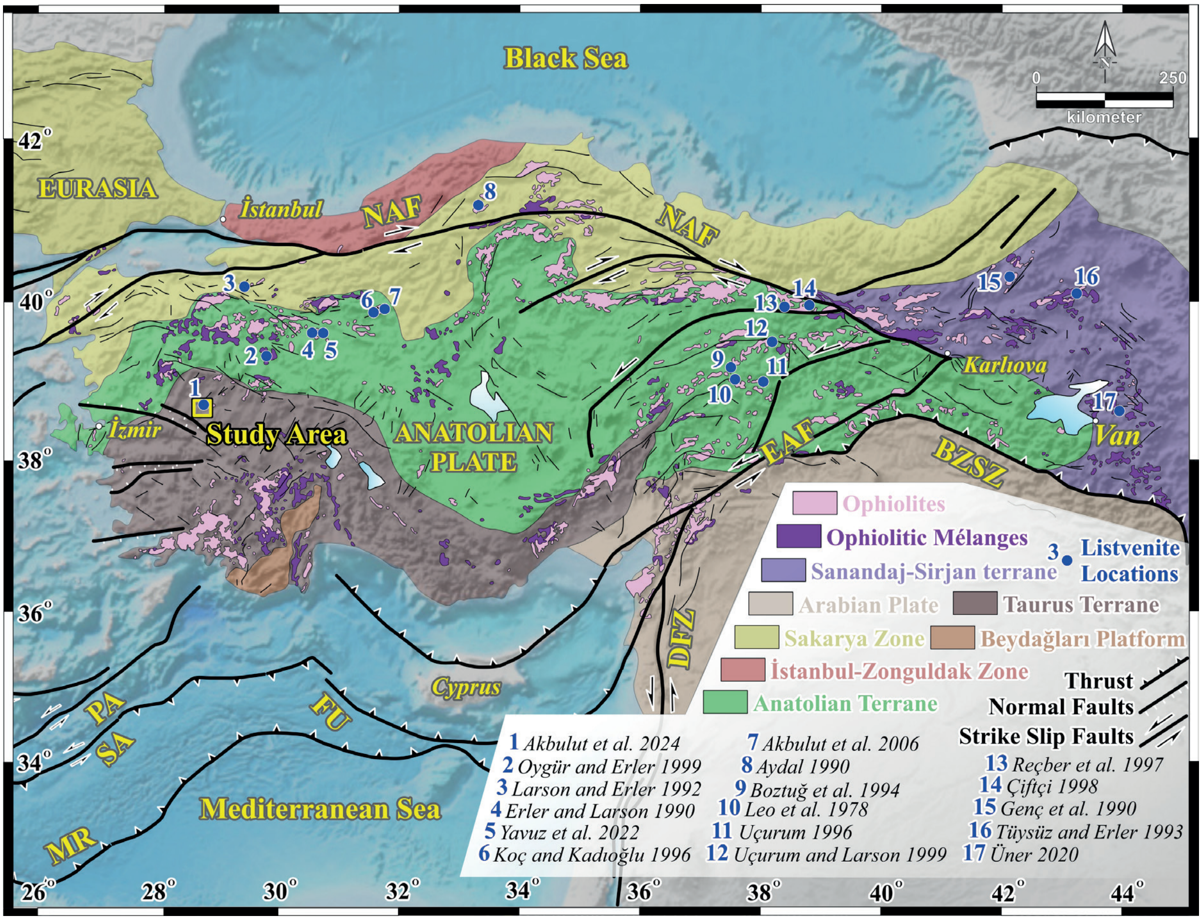

Figure 1. Tectonic map of Turkey and surrounding regions showing locations of the listvenites within serpentinites and serpentinite-matrix mélanges of northern and eastern Turkish ophiolites and the location of the study area. Listvenite locations and tectonic units were compiled based on Moix et al. (2008) and Akbulut et al. (2024) and the references therein. The neotectonic map was modified from Şengör et al. (1985), Barka (1992), Barbot and Weiss (2021), and Bozkurt (2001). Abbreviations: BZSZ – Bitlis-Zagros Suture Zone; DFZ – Dead Sea Fault Zone; EAF – East Anatolian Fault; FU – Florence Uplift; MR – Mediterranean Ridge; NAF – North Anatolian Fault; PA – Pliny Arc; SA – Strabo Arc.

Şekil 1. *Türkiye ve çevresinin, kuzey ve doğu Türkiye ofiyolitlerindeki serpantinitler ve serpantinit matriksli melanjlardan türeyen listvenitlerin konumlarını ve çalışma alanının yerini gösteren tektonik haritası. Listvenit konumları ve tektonik birimler Moix vd. (2008) ve Akbulut vd. (2024) ve orada sunulan referanslardan derlenmiştir. Neotektonik harita Şengör vd. (1985), Barka (1992), Barbot ve Weiss (2021) ve Bozkurt (2001)'den değiştirilerek hazırlanmıştır. Kısaltmalar: BZSZ – Bitlis-Zagros Kenet Kuşağı; DFZ – Ölü Deniz Fay Zonu; EAF – Doğu Anadolu Fayı; FU – Florence Yükselimi; MR – Akdeniz Sırtı; NAF – Kuzey Anadolu Fayı; PA – Pliny Yayı; SA – Strabo Yayı.*

This study aims to map and characterize the listvenite-type hydrothermal/metasomatic alteration minerals in the Kula volcanic field by applying Crosta PCA and band ratio techniques to Landsat 7 ETM+ imagery and to evaluate the spatial relationships between alteration mineral distributions and controlling tectono-volcanic structures in the Manisa-Kula region. The complex lithological assemblages, including serpentinized peridotites with listvenite-type alteration, carbonatized serpentinites, and extensive Quaternary basaltic deposits, provide ideal conditions for spectral discrimination of listvenite-type alteration minerals through an integrated remote sensing approach. With this attempt, we hope to contribute to the literature about remote sensing applications for gossan and similar occurrences in these terrains.

GEOLOGICAL SETTING AND THE STUDY AREA

The Kula-Salihli UNESCO Global Geopark, situated in western Türkiye, is known for its unique Quaternary volcanic landscapes, historically described as “katakekaumene,” or “burnt lands” due to their distinct geomorphological features (Jones, 1929). Geologically, the area is located within the actively extending Gediz Graben system, characterized by significant tectono-stratigraphic complexity and a diverse suite of geological units ranging from ophiolitic mélanges to recent volcanic fields (Ercan and Öztunalı, 1982; Richardson-Bunbury, 1996) (Figure 2).

The study area is underpinned by the ophiolitic mélange, which primarily consists of the completely serpentinized host peridotite unit. This ultramafic unit is locally altered into listvenite horizons, characterized by vertical zonation of a resistant ferruginous silica cap (Fscc) grading downwards into a carbonatized zone (Cnz and CS-Srp) (Figure 2). These basement rocks are unconformably overlain by Pliocene-Miocene sediments (Pms) comprising lacustrine limestone and claystone. The youngest geological features include the Quaternary basaltic volcanics (Qbv) of the Kula Geopark and the recent Quaternary alluvium (Qal) deposits along the Gediz River channel.

The geological framework of the Kula region includes Pre-Mesozoic metamorphic basement rocks overlain tectonically by the Vezirler Mélange, comprising serpentinized peridotites, radiolarites, cherty limestones, and mudstones of Late Cretaceous age (Ercan and Öztunalı, 1982). These ophiolitic rocks are unconformably covered by Pliocene fluvial and lacustrine sediments interbedded with calc-alkaline volcanic extrusions (Ercan and Öztunalı, 1982). The Vezirler Mélange, located in the northeastern part of the Kula region, presents a remarkable exposure of serpentinized peridotites that have undergone extensive carbonatization and silicification, resulting in listvenite-type alteration assemblages (Akbulut et al., 2024) (Figure 2). According to Akbulut et al. (2024), the alteration profile in the northeastern part of the Kula region comprises three principal zones, arranged from bottom to top: a carbonatized and silicified serpentinite (CS-Srp), a coalesced carbonate nodule zone (Cnz), and an iron-oxide-stained silica-carbonate alteration cap (Fscc). At the basal levels, serpentinites exhibit a greenish-white hue and host variably sized carbonate nodules formed during progressive carbonation and silicification processes. The uppermost Fscc zone is characterized by intense silicification and extensive accumulations of iron oxides-oxyhydroxides, primarily hematite and goethite. Within this horizon, carbonates occur as magnesite and dolomite, often preserving the original serpentine fabric. The widespread development of iron oxides and pervasive silicification within the cap are attributed to both intensive meteoric weathering under paleo-surface conditions and introduction of low temperature CO_2-rich geothermal fluid.

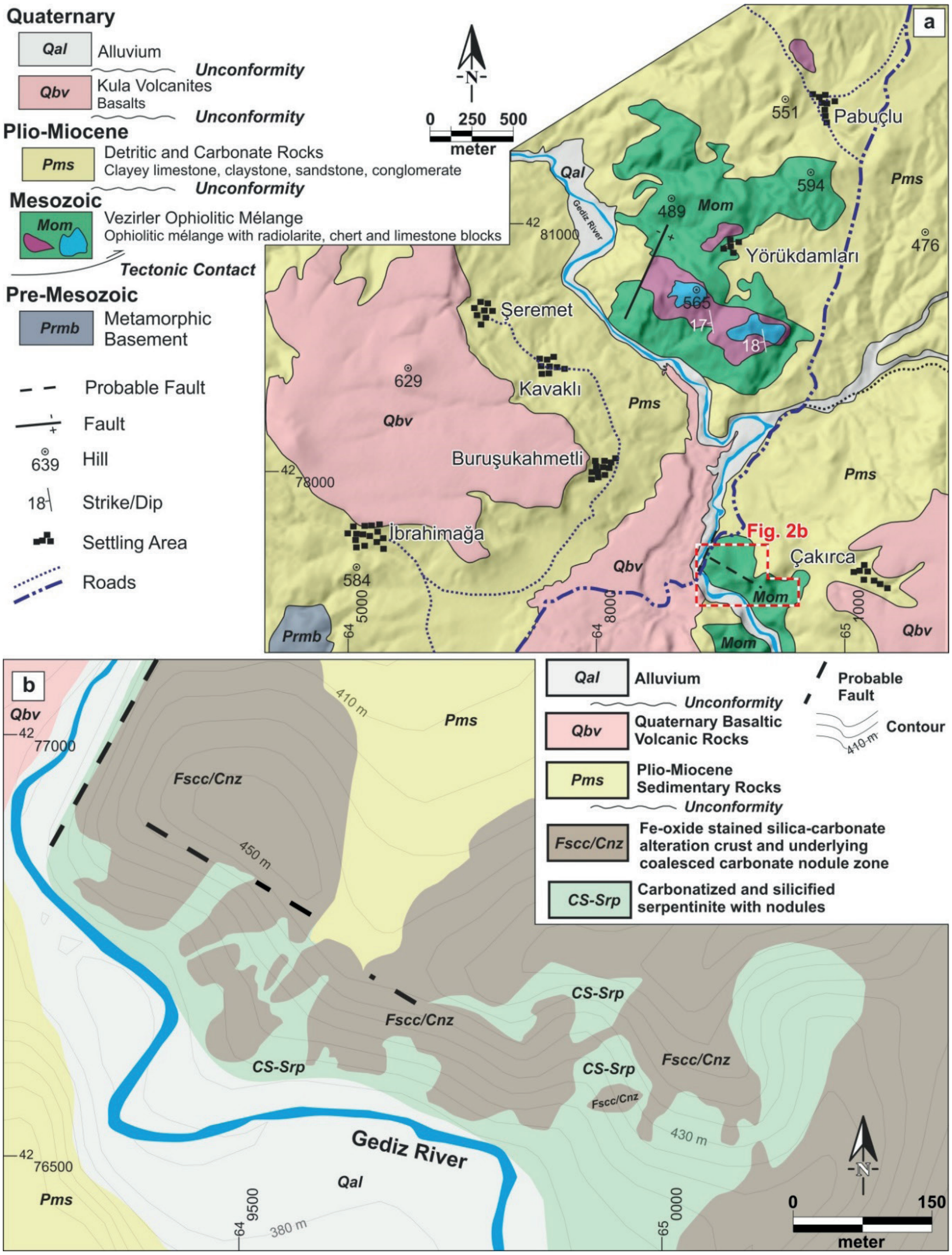

Figure 2. a) Geological map of the northeast of Kula, adapted from Akbulut et al. (2024) based on data from Ercan et al. (1980) and Kılıç et al. (2018). **b)** Detailed geological map of the studied outcrop and its surroundings, adapted from Akbulut et al. (2024). Note: The lithological abbreviations and unit codes defined in this figure are used consistently throughout the manuscript in Figures 4, 5, and 8).

Şekil 2. a) *Ercan vd. (1980) ve Kılıç vd. (2018) verilerine dayanılarak Akbulut vd. (2024)'ten uyarlanan, Kula'nın kuzeydoğusuna ait jeoloji haritası.* ***b)*** *Akbulut vd. (2024)'ten uyarlanan, çalışılan mostranın ve çevresinin ayrıntılı jeoloji haritası. Not: Bu şekilde tanımlanan litolojik kısaltmalar ve birim kodları, makale boyunca Şekil 4, 5 ve 8'de tutarlı bir şekilde kullanılmıştır.*

Quaternary basaltic volcanic extrusions, representing multiple volcanic episodes, dominate the upper stratigraphy, illustrating a regional topographic inversion due to uplift events postdating initial volcanic activity (Richardson-Bunbury, 1996; Tokçaer et al., 2005). Kula volcanism comprises Pliocene-Quaternary alkaline basaltic flows and scoria cones emplaced along structural weaknesses in the normal fault zones bounding the Gediz Graben. This system exhibits a monogenetic character (Şen, 2002). Radiometric dating indicates that eruptive activity commenced following extensional pulses in the early stage at ca. 1.7–2.0 Ma, while Holocene activity is recorded as having ^{40}Ar/^{39}Ar ages of 311 ± 15 ka (Ar-4), 274 ± 13 ka (Ar-3a), and 240 ± 18 ka (Ar-3b) for three successive lava flows (van Gorp et al., 2013). Moreover, ^{3}He exposure ages from western block flows of 1.5 ± 0.3 ka and 2.5 ± 0.4 ka confirm at least two distinct late-Holocene events (Heineke et al., 2016), demonstrating multi-phase volcanism over the last ~ 70 ky. Parallel footwall uplift along the rift axis accelerated from ~ 0.4 mm yr^{-1} in the early phase to ~ 14 mm yr^{-1} at present, reflecting increased eruptive volumes, and high geothermal heat fluxes (> 100 mW m^{-2}) near the northeastern margin of the Gediz Graben corroborate sustained activity (Richardson-Bunbury et al., 2001; Erkan, 2015). This chronological and geodynamic framework indicates that Kula volcanism has evolved through multiple magmatic phases largely independent of regional rifting rates, late-Quaternary climatic fluctuations, and crustal thinning.

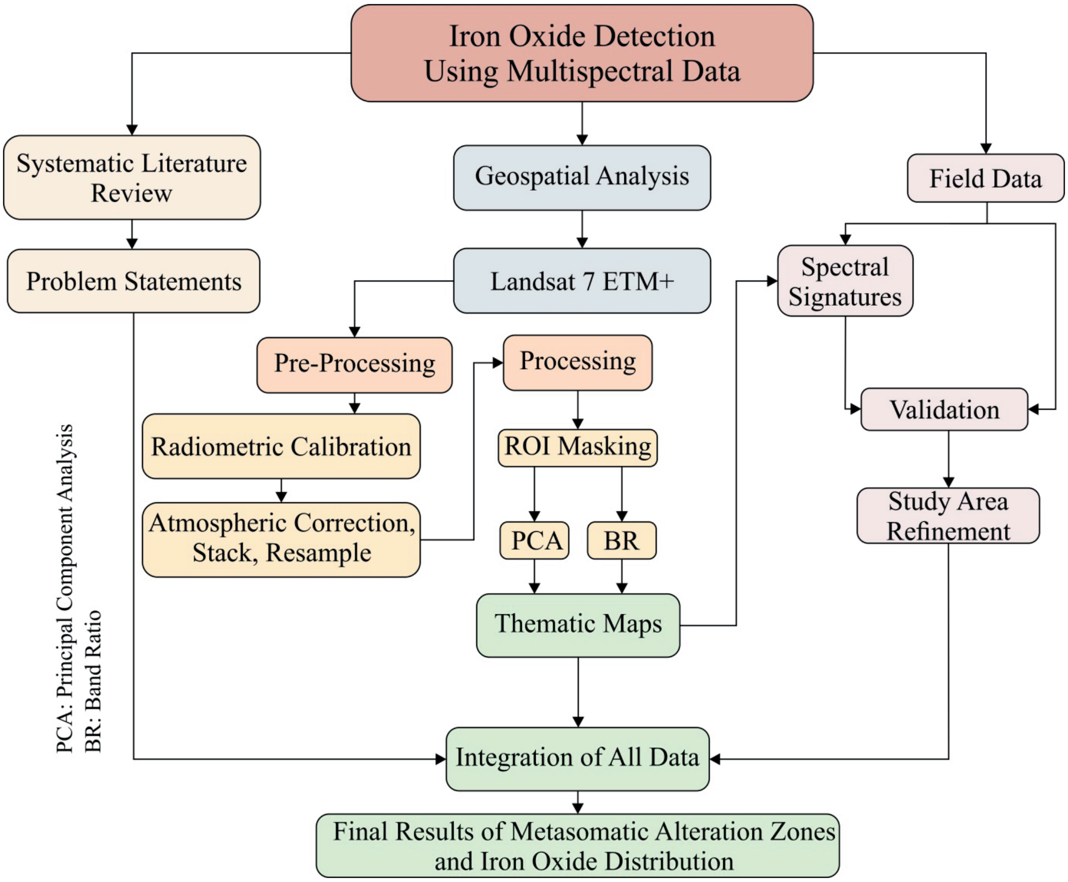

Figure 3. Workflow illustrating the integrated remote sensing approach adopted in this study.

Şekil 3*. Bu çalışmada benimsenen bütünleşik uzaktan algılama yaklaşımını gösteren iş akışı.*

MATERIALS and METHODS

Prior to any field-based investigation, a preliminary remote sensing assessment was conducted using Landsat 7 ETM+ imagery to evaluate the distribution of alteration minerals and iron oxide crust in the broader Kula region. This image-based mineral mapping provided a regional-scale perspective to narrow the study area by identifying zones with prominent spectral anomalies, particularly those indicating iron-bearing and phyllosilicate (hydroxyl bearing sheet silicates - e.g., kaolinite, smectite, serpentine, etc.) altered surfaces. The remote sensing workflow followed during this study is summarized in Figure 3.

To investigate listvenitic metasomatic alteration and iron oxide mineral distributions in the Kula region, Landsat 7 ETM+ imagery dated May 18, 2001, was acquired from the USGS Earth Explorer platform. This pre-2003 scan-line-corrector-on (SLC-on) dataset ensured complete spatial coverage without missing data artifacts. Although contemporary Landsat-8/9 OLI data provide higher radiometric fidelity, the preference for the 2001 Landsat-7 ETM+ dataset is primarily driven by the necessity to analyze lithological exposures prior to recent anthropogenic overprinting. A comparison with modern satellite imagery reveals that significant portions of the target alteration zones have been progressively obscured by expanding agricultural activity and infrastructure development over the last two decades. Consequently, the selected pre-2003 (SLC-on) imagery offers a more pristine spectral record of the geological surface, minimizing non-geological mixing artifacts (e.g., vegetation, man-made structures) that affect modern acquisitions, while ensuring gap-free spatial continuity. Landsat 7 remains widely used in mineral exploration due to its spectral range, including SWIR bands essential for detecting iron oxide and hydroxyl-bearing clay minerals (Van der Meer et al., 2012). The continued relevance of SWIR bands for alteration mapping was also demonstrated in more recent studies utilizing advanced sensors. For example, Johnson and Koperski (2017) applied the 8-band SWIR configuration of the WorldView-3 satellite to successfully distinguish ferric iron and silica alteration zones in the Cuprite mining district, with mapping performance approaching that of hyperspectral AVIRIS data. These findings underscore the importance of SWIR sensitivity, even in multispectral systems such as Landsat 7, for identifying ferruginous and silica-bearing alteration anomalies in geologically complex terrains.

The downloaded Level-1 Terrain Corrected (L1T) imagery was processed in ArcGIS 10.8. First, radiometric calibration was performed to convert digital numbers (DN) to top-of-atmosphere (TOA) radiance using the rescale factors provided in the metadata. Subsequently, an atmospheric correction was applied using the dark object subtraction (DOS1) method (Chavez, 1996) to minimize path radiance effects and retrieve surface reflectance, assuming a uniform haze distribution over the scene. Following these corrections, standard RGB composites were generated by stacking Bands 3 (Red: 0.63–0.69 µm), 2 (Green: 0.52–0.60 µm), and 1 (Blue: 0.45–0.52 µm). These visual composites provided a preliminary basis for distinguishing volcanic units and sedimentary contacts based on color tone and texture. To enhance spatial detail for visual interpretation, the RGB composite was pan-sharpened using the 15 m panchromatic Band 8, yielding improved delineation of structural and lithological boundaries (Rencz and Ryerson, 1999). It should be noted that this pan-sharpened product was utilized solely for qualitative visualization; all subsequent quantitative analyses (PCA and band ratios) were performed on the original 30 m multispectral datasets to preserve spectral fidelity.

To delineate the listvenite alteration zones and isolate specific mineralogical anomalies, a selective principal component analysis (selective PCA) approach adapted from the feature-oriented logic of the Crosta technique (Crosta and Moore, 1989) was employed alongside standard band ratio methods (Table 1). Unlike standard PCA applied to the entire band stack, this selective approach processes specific two-band subsets to maximize the spectral contrast between target mineral absorption and background reflectance. The selection of the specific principal component (PC) for alteration mapping was guided by the inspection of eigenvector loadings, following the Crosta technique (Crosta and Moore, 1989). In all selective PCA subsets (e.g., Bands 1+3, 4+5, 5+7), PC1 exhibited high positive loadings for both input bands, mapping standard scene brightness (albedo) and topography. In contrast, PC2 displayed eigenvector loadings with opposite signs, capturing the spectral variance attributable to mineralogical features. Consequently, PC2 was identified as the relevant component containing specific spectral information for Fe^{3+}, Fe^{2+}, and hydroxyl-bearing minerals, respectively. Two separate selective PCA runs were conducted in this study. The first utilized a subset of Bands 5 (1.55–1.75 µm) and 7 (2.08–2.35 µm) to enhance responses from hydroxyl-bearing phyllosilicates such as kaolinite, smectite, and serpentine. In this configuration, the second principal component (PC2) captures the spectral contrast between the high reflectance in Band 5 and the absorption features in Band 7. The second run used Bands 1 (0.45–0.52 µm) and 3 (0.63–0.69 µm) to highlight Fe^{3+} iron oxides like hematite and goethite, exploiting the strong charge-transfer absorption in the blue region (Band 1) versus high reflectance in the red region (Band 3).

To increase the sensitivity of PCA to localized alteration features and suppress spectral interference from non-target lithologies, a spatial masking strategy was implemented prior to statistics calculation. Individual spectral bands were first clipped using a field-verified region-of-interest (ROI) shapefile enclosing the host serpentinized peridotites and ferruginous outcrops. This spatial masking strategy was deliberately designed to exclude the Gediz River channel and adjacent agricultural lowlands; thereby functioning as an effective manual filter against water (NDWI) and vegetation (NDVI) spectral interference without the need for global statistical thresholding. This targeted approach, similar to the masking-based technique implemented by Liu et al. (2011), effectively reduced spectral dilution from surrounding vegetation and alluvium. Consequently, this step enhanced the anomaly contrast in the resulting PC2 images by limiting the statistical calculation to geologically relevant zones.

Table 1. Spectral indices and PCA configurations used for detecting listvenite-type alteration minerals based on Landsat 7 ETM+ imagery.

Çizelge 1. *Landsat 7 ETM+ görüntülerine dayalı olarak listvenit-tipi alterasyon minerallerini saptamak için kullanılan spektral indeksler ve PCA konfigürasyonları.*

Index Type	PCA	Band Ratio	Spectral Logic (ETM+)	Targets
Iron oxide (Fe^{3+})	B1, B3	B3/B2	High Red reflectance (B3) vs. Green absorption wing (B2)	Hematite (α-Fe_2O_3), Goethite (α-FeOOH)
Ferrous iron (Fe^{2+})	B4, B5		Contrast between NIR (B4) and SWIR1 (B5) variance	Magnetite, Siderite
Phyllosilicate (OH^-)	B5, B7	B5/(B5 + B7)	High SWIR1 reflectance (B5) vs. SWIR2 Al-OH absorption (B7)	Kaolinite, Illite, Smectite, Serpentine
Silica alteration	B5, B7	B7/B5	Suppression of OH absorption; inverse of clay response	Silicified serpentinite, quartz veins

Complementing the PCA analysis, three specific spectral band-ratio indices were computed to map ferric iron, silica, and hydroxyl-bearing phases. These indices were selected based on the specific reflectance and absorption physics of the target minerals (Table 1). (1) Ferric Iron (Fe^{3+}) Index (Band 3 / Band 2): This ratio highlights hematite and goethite by exploiting their characteristic high reflectance in the red region (0.63–0.69 µm, Band 3) contrasted against the charge-transfer absorption wing present in the green region (0.52–0.60 µm, Band 2) (Segal, 1982). (2) Hydroxyl (OH^-) Index (Band 5 / (Band 5 + Band 7)): This formula targets phyllosilicates (e.g., kaolinite, smectite) by enhancing the high reflectance in SWIR1 (1.55–1.75 µm, Band 5) relative to the diagnostic Al-O-H vibrational absorption feature centered in SWIR2 (2.08–2.35 µm, Band 7) (Aydal et al., 2007). (3) Silica Index (Band 7 / Band 5): Used as a proxy for silicified zones, this ratio highlights areas where the diagnostic SWIR2 absorption of clays is absent or suppressed due to intense silicification, resulting in relatively higher Band 7 values compared to Band 5 (Kayadibi, 2008). In addition to enhancing spectral features, these band ratios were employed to mitigate varying illumination effects caused by the rugged topography, as the topographic slope factor tends to be cancelled out in the ratio calculation (Lillesand et al., 2015). It is important to note that a simple band ratio was not employed for ferrous iron (Fe^{2+}) due to the spectral complexity and broad absorption features of ferrous minerals in the NIR-SWIR range; instead, this target was mapped exclusively using the selective PCA method (PC2 of Bands 4 and 5) to maximize subtle variance. To facilitate objective interpretation and anomaly ranking, the resulting ratio maps were statistically segmented using mean (μ) and standard deviation (σ) thresholds derived exclusively from the masked image subsets within the field-verified region (Figure 2b). Specifically, pixels with values exceeding $\mu + \sigma$ were categorized as high anomalies, those falling between $\mu - \sigma$ and $\mu + \sigma$ were defined as moderate anomalies (representing background variance), and values below $\mu - \sigma$ were classified as low anomalies. This classification method, widely applied in alteration mapping (Tangestani and Moore, 2001; Enoh et al., 2021), allowed the pixel values to be categorized into distinct intensity classes as detailed in Table 2. The statistical parameters were calculated from a sample size of N = 925 pixels (approximately 0.83 km²). Sensitivity testing indicated that a narrower threshold ($\mu \pm 0.5\sigma$) resulted in excessive background noise (false positives), while a stricter threshold ($\mu \pm 1.5\sigma$) omitted verified peripheral alteration zones. Therefore, the $\mu \pm 1.0\sigma$ interval was selected as the optimal discriminator for this geological setting.

Field investigations were conducted following the interpretation of satellite spectral data to validate alteration zones and refine geological boundaries. Spectral anomalies identified through PCA and band ratio analyses, particularly zones with strong Fe^{3+} responses or OH^- bearing signatures, were prioritized for ground verification (Figure 4). Field verification focused on the northeastern sector of the study area, where previous studies reported extensive silica-carbonate and iron oxide alteration in detail (Akbulut et al., 2024).

Table 2. Statistical classification thresholds for band ratio indices.

Çizelge 2. *Bant oranı indeksleri için istatistiksel sınıflandırma eşikleri.*

Index	Low Anomaly ($<\mu - \sigma$)	Moderate Anomaly ($\mu \pm \sigma$)	High Anomaly ($>\mu + \sigma$)	Interpretation
Fe^{3+}	< 1.01	1.01 – 1.15	> 1.15	Hematite–goethite enrichment, iron stained serpentinite
Silica	< 0.693	0.693 – 0.775	> 0.775	Silicification, quartz veins, silica-carbonate crusts
OH^-	< 0.563	0.563 – 0.591	> 0.591	Kaolinite–smectite alteration, clay-rich zones

The mineralogical identities of the mapped units (e.g., magnesite, dolomite, quartz, hematite) were cross-referenced with the detailed XRD and petrographic data provided in Akbulut et al. (2024) to ensure accurate spectral attribution. During fieldwork, outcrops exhibiting surface staining, pervasive silicification, or ferruginous coatings were examined. Field notes, photographs, and handheld GPS locations were recorded and imported into GIS to compare with remote sensing outputs. Additionally, lithological boundaries observed in the field such as the transition from carbonatized serpentinite to overlying silica-iron alteration caps were digitized. This allowed refinement of unit contacts and the delineation of altered zones with higher positional accuracy. Observations of carbonate nodules, brecciated serpentinite, and weathered iron oxide-stained silica-carbonate crust supported the spectral interpretations derived from satellite models. This approach ensured that remotely sensed data were not only validated but also geologically meaningful within the regional tectonic and volcanic framework.

Figure 4. Field photographs showing vertical and lateral transitions between alteration zones in NE Kula: **a)** outcrop-scale contact between CS-Srp and Fscc/Cnz, **b)** close-up of the Cnz-Fscc boundary, and **c)** resistant Fscc cap over friable Cnz and underlying serpentinized bedrock.

Şekil 4. *KD Kula'daki alterasyon zonları arasındaki düşey ve yanal geçişleri gösteren arazi fotoğrafları:* ***a)*** *CS-Srp ve Fscc/Cnz arasındaki mostra ölçekli dokanak,* ***b)*** *Cnz-Fscc sınırının yakından görünümü ve* ***c)*** *Ufalanabilir Cnz ve altındaki serpantinleşmiş temel kaya üzerindeki dirençli Fscc şapkası.*

RESULTS

Landsat-Based Regional Alteration Patterns

The implementation of the exclusionary ROI mask significantly refined the spatial extent of the mapped anomalies. In preliminary unmasked processing, the Gediz fluvial corridor and vegetated northern slopes exhibited diffuse, noise-dominated spectral responses that obscured genuine geological features. The application of the mask effectively truncated these false positives, ensuring that the high-anomaly clusters described below are strictly associated with bedrock lithology rather than riparian vegetation or moisture-saturated alluvium. Within the masked domain, the Fe^{3+}-sensitive PC2 component (derived from Bands 1 and 3) reveals clear anomaly clusters associated with carbonatized and silicified serpentinites and iron oxide–bearing crust fragments, most prominently along the eastern margin of the ophiolitic outcrops (Figure 5a). These patterns agree with field observations documenting pervasive ferric-iron staining and hematite-coated surfaces (Figure 4).

To validate the spectral results with ground observations, PC2 outputs were examined within the field-confirmed ROI (Figure 2b). In this zone, elevated PC2 values remain concentrated along ridge crests and resistant cap exposures, consistent with a localized alteration footprint. The ROI histogram shows a right-skewed distribution toward high PC2 values ($\mu = 40.59$, $\sigma = 5.24$, Range: 29–66) (Figure 5b), supporting localized but spectrally intense ferric enrichment. A secondary anomaly south–southwest of the ROI (inset in Figure 5a) also coincides with serpentinite outcrops. The spectral intensity of this feature mirrors the response observed in the field-verified northern sector, suggesting the presence of a similar but previously unmapped iron-oxide bearing alteration zone. Therefore, rather than being a background artifact, this area is identified as a priority target for future ground-based exploration to verify the extension of the listvenite system.

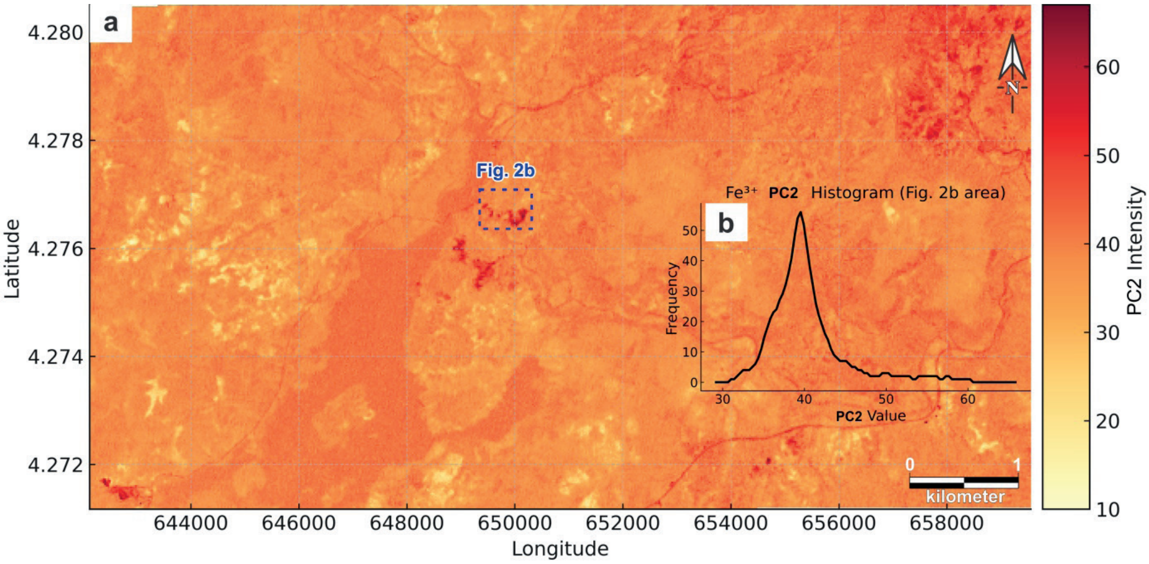

Figure 5. a) Regional-scale masked PC2 map derived from Landsat-7 ETM+ Bands 1 and 3 (Fe^{3+}-sensitive PCA). (Acquisition Date: 18 May 2001; SLC-on). **b)** Histogram of PC2 values calculated specifically within the field-verified ROI (Fig. 2b).

Şekil 5. a) *Landsat-7 ETM+ Bant 1 ve 3 kullanılarak türetilen (*Fe^{3+}*-duyarlı PCA) Bölgesel ölçekli Maskelenmiş PC2 haritası (Görüntü Tarihi: 18 Mayıs 2001; SLC-on).* ***b)*** *Arazi doğrulamalı ROI (Şekil 2b) içindeki PC2 değerlerinin histogramı.*

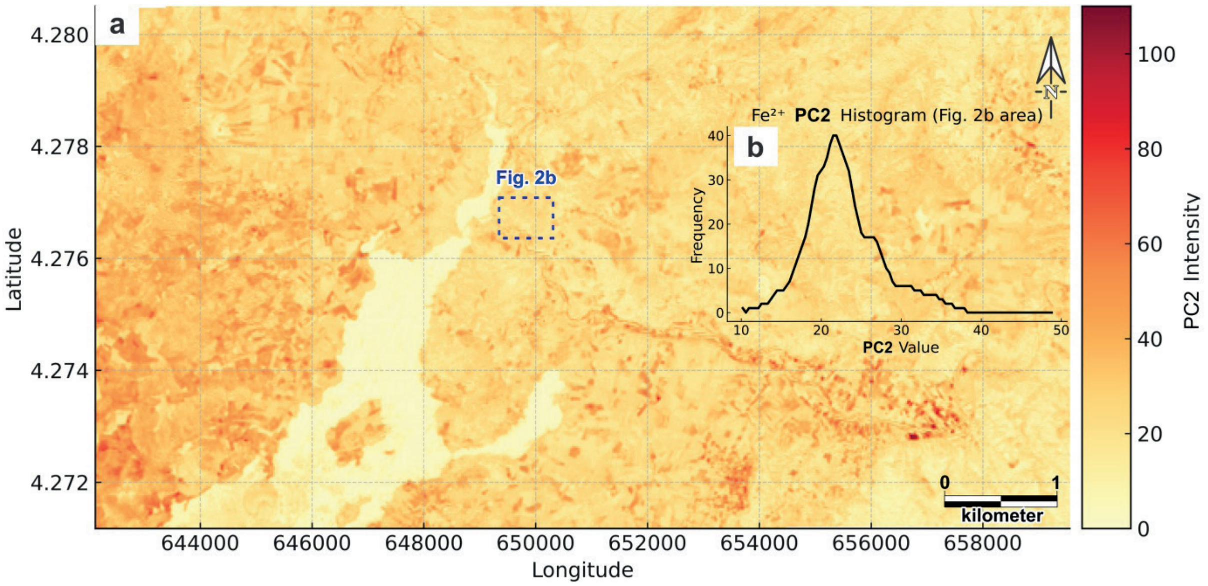

Figure 6. a) Regional-scale masked PC2 map derived from Landsat-7 ETM+ Bands 4 and 5 (Fe^{2+}-sensitive PCA). (Acquisition Date: 18 May 2001; SLC-on). **b)** Histogram of PC2 values calculated specifically within the field-verified ROI (Fig. 2b).

Şekil 6. a) *Landsat-7 ETM+ Bant 4 ve 5 kullanılarak türetilen (Fe^{2+}-duyarlı PCA) Bölgesel ölçekli Maskelenmiş PC2 haritası (Görüntü Tarihi: 18 Mayıs 2001; SLC-on).* ***b)*** *Arazi doğrulamalı ROI (Şekil 2b) içindeki PC2 değerlerinin histogramı.*

Compared to the Fe^{3+} response, the Fe^{2+}-sensitive PC2 (derived from Bands 4 and 5) exhibits lower spectral contrast overall (Figure 6a). While scattered zones of enhanced response appear in mafic-rich domains, these features likely reflect mixed mafic mineralogy rather than distinct alteration, as spectral overlap limits discrimination at 30 m resolution. Within the field-confirmed ROI, PC2 values are notably subdued ($\mu = 23.02$, $\sigma = 5.02$, Range: 10–49) (Figure 6b), suggesting that ferrous phases are largely oxidized or overprinted in the most altered surfaces.

The strongest patterns were obtained from the OH-sensitive PC2 (derived from Bands 5 and 7). This component delineates alteration halos compatible with hydroxyl-bearing phyllosilicate assemblages (e.g., kaolinite, smectite, serpentine) around listvenite crusts and volcanic edifices (Figure 7a). Notably, the field-confirmed ROI exhibits a relatively subdued OH response; this is interpreted to reflect strong silicification and iron-oxide dominance that suppress diagnostic hydroxyl absorption features. Consequently, the ROI histogram appears broad and relatively flat ($\mu = 27.74$, $\sigma = 2.70$, Range: 15–35) (Figure 7b), indicating spatially variable hydroxyl signatures in this highly altered domain.

Additional Indices Supporting PCA-Band Ratio

In addition to PCA analysis, three band-ratio indices were computed for the ROI to highlight spectrally distinct alteration features (Figure 8a–d). The Fe^{3+} index map (B3/B2) emphasizes ferric-oxide contrast, with high values clustering along the eastern margins of the Fscc/Cnz unit and matching field-mapped hematitic coatings (Figure 8a). Lower index values in the sedimentary (Pms) and volcanic (Qbv) units differ from the alteration zones, consistent with weaker oxidation signatures. The silica index (B7/B5) identifies zones of elevated SWIR2/SWIR1 contrast, with the highest values occurring along the southern boundary of Fscc/Cnz where quartz veinlets and siliceous crusts were observed (Figure 8b). The hydroxyl index [B5/(B5 + B7)] highlights clay-rich weathering fronts along the northwestern margins of the CS-Srp unit, whereas the siliceous Fscc/Cnz caps exhibit lower values due to the suppression of hydroxyl features (Figure 8c).

To enhance interpretability, ratio outputs were statistically segmented using mean (μ) and standard deviation (σ) values derived from the ROI. Pixels above μ + σ were classified as high anomalies and generally coincide with the most intense alteration surfaces mapped in the field, whereas pixels below μ − σ represent background domains. When integrated with the lithological framework (Figure 8d), these segmented maps confirm that spectral signatures are systematically constrained by the lithological and structural controls observed in the field. Quantitative zonal statistics derived from the PC2 datasets further validate this correspondence. For the ferric iron (Fe^{3+}) component, the iron-oxide stained Fscc/Cnz unit exhibits a significantly elevated mean value (μ = 46.81), with approximately 58.8% of its area classified as high anomaly (> μ + σ). In sharp contrast, the underlying CS-Srp unit has a much lower mean response (μ = 38.97) with only 8.1% of pixels exceeding the anomaly threshold, quantitatively confirming the method's efficacy in discriminating the alteration cap from the host rock. Furthermore, the hydroxyl (OH^-) response is slightly suppressed in the Fscc/Cnz unit (14.2% anomaly coverage) compared to the CS-Srp unit (17.9%), consistent with the masking of phyllosilicate features by intense silicification and iron-oxide coatings.

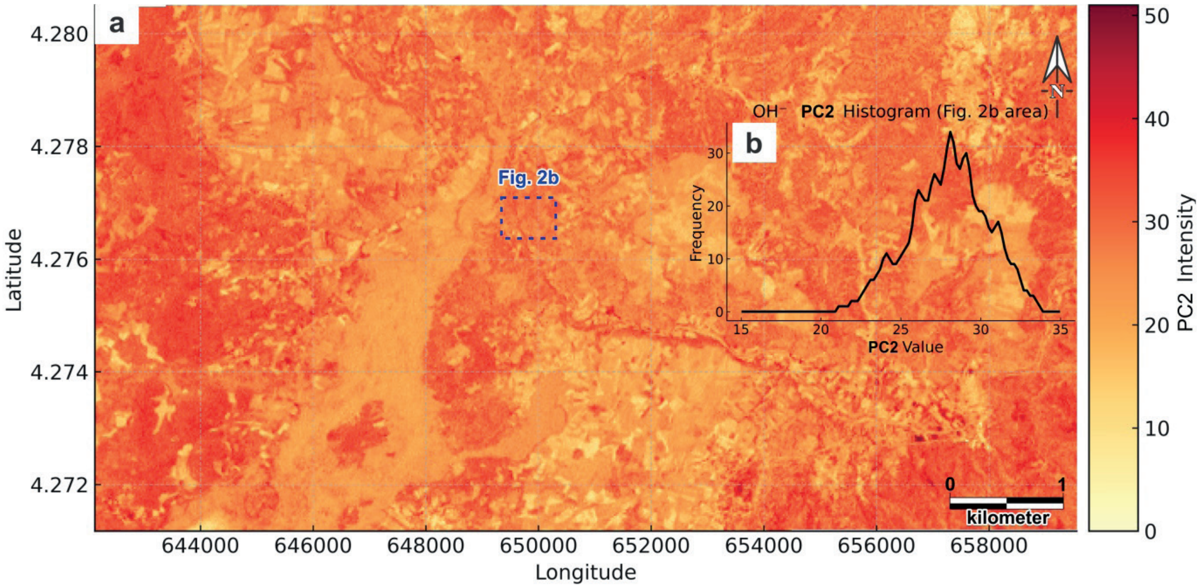

Figure 7. a) Regional-scale masked PC2 map derived from Landsat-7 ETM+ Bands 5 and 7 (OH^-/phyllosilicate-sensitive PCA). (Acquisition Date: 18 May 2001; SLC-on). **b)** Histogram of PC2 values calculated specifically within the field-verified ROI (Fig. 2b).

Şekil 7. a) *Landsat-7 ETM+ Bant 5 ve 7 kullanılarak türetilen (OH^-/fillosilikat-duyarlı PCA) Bölgesel ölçekli Maskelenmiş PC2 haritası (Görüntü Tarihi: 18 Mayıs 2001; SLC-on).* ***b)*** *Arazi doğrulamalı ROI (Şekil 2b) içindeki PC2 değerlerinin histogramı.*

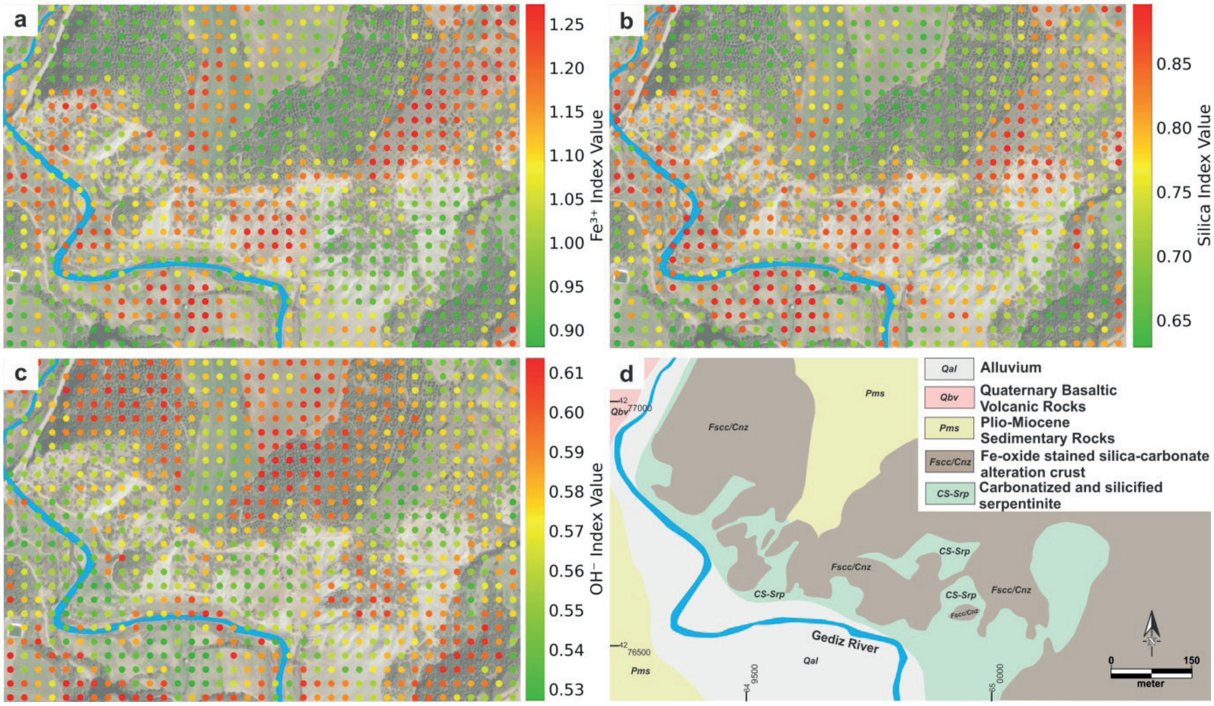

Figure 8. Band-ratio index maps overlayed on Fig. 2b ROI: **a)** Fe^{3+} index (B3/B2) (unitless), **b)** silica index (B7/B5) (unitless), **c**) OH^- index (B5/(B5 + B7)) (unitless), and **d**) geological map of the ROI with lithological boundaries and unit labels (adapted from Akbulut et al., 2024). (Landsat-7 ETM+ Acquisition Date: 18 May 2001; SLC-on).

***Şekil 8**. Şekil 2b ROI üzerinde bant-oranı indeks haritaları: **a)** Fe^{3+} indeksi (B3/B2), **b)** silis indeksi (B7/B5), **c)** OH^- indeksi (B5/(B5 + B7)), **d)** ROI'nin litolojik sınırlarını ve birim etiketlerini gösteren jeoloji haritası (Akbulut vd. 2024'ten uyarlanmıştır).*

DISCUSSION AND CONCLUSION

Methodologically, the results confirm that targeted selective PCA plus μ ± σ-segmented indices is a robust, scalable approach for rapid screening in complex ophiolitic–volcanic terrains. ROI masking prior to PCA increases signal-to-noise by excluding non-diagnostic spectral variability, while ratio-based thresholds translate continuous gradients into operationally interpretable classes that can be ranked for field validation or geochemical sampling (Liu et al., 2011; Tangestani and Moore, 2001). Nevertheless, several limitations must be acknowledged. First, the Landsat 7 ETM+ sensor lacks a dedicated spectral band in the 0.9–1.0 μm range (unlike ASTER Band 4), which significantly limits its sensitivity to the diagnostic crystal field absorptions of ferrous iron (Fe^{2+}) minerals. Additionally, multispectral (30 m) spatial resolution promotes sub-pixel mixing in thin alteration veneers; strong Fe^{3+} coatings can spectrally dominate over Fe^{2+} and OH features, and shadow/moisture in valley floors can mask weak anomalies along the Gediz fluvial corridor. These caveats explain muted hydroxyl responses in the most silicified listvenite caps and the under-expression of Fe^{2+} where oxidation is advanced (van der Meer et al., 2012).

While this workflow offers a robust, zero-cost solution for regional exploration, practitioners must acknowledge that the spectral signatures can be masked by environmental factors such as dense vegetation cover, extensive lichen growth, or desert varnish on rock surfaces. In these scenarios, or where detailed mineralogical discrimination (e.g., distinguishing specific clay species) is required, the broad bandwidths of Landsat ETM+

may be insufficient. In these cases, sensors with higher spectral resolution, such as ASTER (SWIR/TIR) or commercial high-spatial-resolution platforms like WorldView-3, are preferable alternatives, albeit at the expense of data cost and processing complexity. Therefore, the proposed Landsat-based method is best utilized as a first-pass screening tool to prioritize targets for more capital-intensive follow-up surveys.

A sensor-to-sensor comparison using Landsat-8/9 OLI (and Sentinel-2) remains a logical next step for monitoring modern surface changes, but it requires sensor-specific selective PCA tuning and threshold re-derivation to ensure consistent PC behavior across instruments. Looking forward, pairing Landsat-class VNIR–SWIR coverage with higher spectral-fidelity SWIR/TIR (e.g., ASTER TIR and archival ASTER SWIR scenes acquired prior to 2008) or contemporary multispectral–hyperspectral assets would sharpen mineral discrimination (e.g., kaolinite vs. illite vs. serpentine; silica polymorphs) and further deconvolve ferric coatings from clay signatures. Recent workflows that merge Landsat-8 with ASTER exploit complementary bandsets to enhance alteration mineral mapping and lineament analysis, an approach well suited to the Kula domain (Orynbassarova et al., 2025).

In conclusion, ROI-masked selective PCA isolated ferric-iron and hydroxyl-bearing anomalies that correspond closely with field-mapped Fscc/Cnz caps and CS-Srp units, whereas Fe^{2+} responses were weak where oxidation is advanced (Tangestani and Moore, 2001). The $\mu \pm \sigma$-segmented Fe^{3+} (> 1.15), silica (> 0.775), and OH^- (> 0.591) indices provided objective thresholds that validate PCA outputs and revealed additional targets for ground verification (Enoh et al., 2021). The mapped alteration architecture is consistent with listvenite formation pathways and highlights sites of potential economic and CCS-relevant interest in the Kula ophiolitic mélange (Uçurum, 2000; Akbulut et al., 2024).

ACKNOWLEDGEMENTS

The authors would like to thank the reviewers for their constructive comments that enhanced the quality of the paper. We are also sincerely grateful to Onur Altun for his assistance with the remote sensing data processing and fieldwork.

DATA AVAILABILITY STATEMENT

Data Availability Statement The satellite imagery data that support the findings of this study are openly available from the U.S. Geological Survey (USGS) EarthExplorer (https://earthexplorer.usgs.gov), specifically the Landsat 7 ETM+ scene acquired on 18 May 2001 (SLC-on). The vector data (ROI shapefiles), calculated zonal statistics spreadsheets, and the detailed processing parameters supporting the conclusions of this article are available from the corresponding author upon reasonable request.

GENİŞLETİLMİŞ ÖZET

Bu çalışma, Batı Türkiye'deki Kula bölgesinde yer alan Vezirler ofiyolitik melanjındaki listvenit tipi silis-karbonat alterasyon zonlarını haritalamak amacıyla, düşük maliyetli ve bütünleşik bir uzaktan algılama iş akışının etkinliğini değerlendirmektedir. Altın, gümüş ve kobalt gibi ekonomik potansiyellerinin yanı sıra küresel iklim krizi ile mücadelede doğal Karbon Yakalama ve Depolama (CCS) süreçlerinin analogları olmaları sebebiyle bertaraf stratejilerinin geliştirlmesi için de önem taşıyan bu mineralizasyonların belirlenmesi ve haritalanması önemlidir. Çalışma, özellikle vejetasyon ve alüvyal örtüden kaynaklanan spektral karışıklıkları minimize ederek, demir oksit ve hidroksil içeren alterasyon şapkalarını (demir şapkaları) serpantinleşmiş yan kayaçlardan ayırt etmeyi hedeflemiştir.

Yöntem olarak, antropojenik bozulmanın en az olduğu dönemi temsil etmesi nedeniyle 18 Mayıs 2001 tarihli, tarama hatası içermeyen (SLC-on) bir Landsat-7 ETM+ görüntüsü kullanılmıştır. Ofiyolitik arazilerde sıkça karşılaşılan spektral

gürültüyü gidermek amacıyla, Gediz Nehri koridorunu ve tarımsal alanları dışlayan litoloji tabanlı bir "İlgi Alanı (ROI)" maskeleme stratejisi uygulanmıştır. Bu maskelenmiş veri seti üzerinde, Crosta Tekniğine dayalı Seçici Temel Bileşenler Analizi (Selective PCA) ve tamamlayıcı bant oranlama yöntemleri (Fe^{3+}, Fe^{2+}, OH^{-} ve Silis) uygulanmıştır. Elde edilen spektral anomaliler, arazi çalışmaları ve petrografik/XRD verileriyle (Akbulut vd., 2024) doğrulanmış; sonuçlar Ortalama ± Standart Sapma ($\mu \pm \sigma$) eşik değerleri kullanılarak istatistiksel olarak sınıflandırılmıştır. Hassasiyet analizleri, $\mu \pm 1.0\sigma$ eşik değerinin, gürültü (yanlış pozitifler) ile gerçek jeolojik sınırları ayırmada en optimum aralık olduğunu göstermiştir.

Elde edilen bulgular, ROI maskeli Seçici PCA yönteminin alterasyon zonlarını ayırt etmede yüksek bir başarı sağladığını göstermektedir. Özellikle Fe^{3+} duyarlı PC2 bileşeni (Bant 1 ve 3'ten türetilen), arazide gözlenen hematit kaplı demirli silis şapkaları (Fscc/Cnz) ile güçlü bir mekansal uyum sergilemiştir. Bölgesel istatistiksel analizler (Zonal Statistics), yöntemin başarısını nicel olarak da kanıtlamaktadır: Hedeflenen alterasyon şapkası (Fscc/Cnz) ortalama μ=46,81 değeriyle alanın %58,8'inde "Yüksek Anomali" verirken, altere olmamış serpantin yan kayacında (CS-Srp) bu oran sadece %8,1 olarak hesaplanmıştır. Aradaki bu belirgin fark, yöntemin hedef kütleyi yan kayaçtan başarıyla ayırdığını doğrulamaktadır. Buna karşın, Fe^{2+} anomalileri (Bant 4 ve 5), Landsat sensörünün spektral çözünürlük kısıtları ve yüzeydeki yoğun oksidasyon örtüsü nedeniyle daha sınırlı bir tespit başarısı göstermiştir. Hidroksil (OH^{-}) haritalaması ise fillosilikatça zengin zonları belirlemiş, ancak yoğun silisleşmiş şapka kısımlarında kil minerallerinin bozulması veya maskelenmesi nedeniyle anomali değerlerinin beklendiği üzere düştüğü (%14,2) gözlemlenmiştir.

Sonuç olarak bu çalışma, dışlayıcı maskeleme ve hedefe yönelik PCA teknikleriyle işlenen Landsat-7 verilerinin, yarı kurak ofiyolitik kuşaklarda listvenit arama çalışmaları için sağlam ve maliyet etkin bir tarama aracı olduğunu ortaya koymaktadır. Yöntem, özellikle demirce zengin alterasyon şapkalarını çevre kayaçlardan istatistiksel olarak anlamlı bir doğrulukla ayırabilmektedir. Çalışma, belirlenen spektral eşik değerlerinin saha çalışmalarını önceliklendirmek için objektif bir kriter sağladığını göstermekle birlikte; gelecekteki çalışmalarda spesifik kil türlerinin veya düşük tenörlü Fe^{2+} minerallerinin ayrımı için ASTER (SWIR/TIR) veya WorldView-3 gibi daha yüksek spektral çözünürlüklü sensörlerin entegre edilmesini önermektedir.

ORCID

Semih Eski https://orcid.org/0000-0002-2526-2571
Mehmet Akbulut https://orcid.org/0000-0002-4869-5249

REFERENCES / *KAYNAKLAR*

Abrams, M. J., Brown, D., Lepley, L. & Sadowski, R. (1983). Remote sensing for porphyry copper deposits in Southern Arizona. Economic Geology, 78, 591-604. https://doi.org/10.2113/gsecongeo.78.4.591

Akbulut, M., Pişkin, Ö. & Göncüoğlu, M. C. (2006). Genesis of the carbonatized and silicified rocks (listwaenites) as a result of alteration of ultramafics, Mihalıççık region, NW Turkey. *Geological Journal, 41*(5), 557–580. https://doi.org/10.1002/gj.1058

Akbulut, M., Tokcaer, M. & Büçkün, Z. (2024). Carbonatization and silicification of peridotites within the Vezirler ophiolitic mélange (Kula-Manisa, Western Türkiye): A natural analogue for CO_2 sequestration. *Ofioliti, 49*(2). https://doi.org/10.4454/ofioliti.v49i2.569

Aydal, D. (1990). Gold-bearing listwaenites in the Arac massif, Kastamonu, Turkey. *Terra Nova,* 2, 43–52. https://doi.org/10.1111/j.1365-3121.1990.tb00035.x

Aydal, D., Vural, A., Taşdelen, İ. U. & Aydal, E. G. (2007). Alakeçi-Kısacık (Bayramiç-Balıkesir) Cevherleşme Bölgesinin Landsat 7 Etm+ Kullanılarak Crosta Tekniği ile İncelenmesi, *Selçuk Üniversitesi Mühendislik, Bilim ve Teknoloji Dergisi, 22*(3), 29-40.

Aytaç, A. S. & Demir, T. (2023). The Kula–Salihli UNESCO Geopark: Spectacular records of Quaternary volcanism, fluvial and landscape evolution and Quaternary environmental change. *Proceedings of the Geologists' Association, 134(4)*, 416–431. https://doi.org/10.1016/j.pgeola.2022.08.002

Barbot, S. & Weiss, J. R. (2021) Connecting subduction, extension and shear localization across the Aegean Sea and Anatolia. *Geophysical Journal International, 226*(1), 422-445. https://doi.org/10.1093/gji/ggab078

Barka A. A. (1992). The north Anatolian Fault Zone. *Annales Tectonicae, 6*, 164-165.

Binal, A. & Ercanoğlu, M. (2010). Assessment of rockfall potential in the Kula (Manisa, Turkey) Geopark Region. *Environmental Earth Sciences, 61*(7), 1361–1373. https://doi.org/10.1007/s12665-010-0454-1

Bishop, J. L., Fröschl, H. & Mancinelli, R. L. (1998). Alteration processes in volcanic soils and identification of exobiologically important weathering products on Mars using remote sensing. *Journal of Geophysical Research, 103(E13)*: 31457–31476. https://doi.org/10.1029/1998JE900008

Bozkurt, E. (2001). Neotectonics of Turkey – a synthesis. *Geodinamica Acta, 14*(1-3), 3-30. https://doi.org/10.1016/S0985-3111(01)01066-X

Boztuğ, D., Harlavan, Y., Arslan, M. & Temizel, I. (1994). Geological setting, mineralogy and precious metal content of the listwaenitic rocks in the Alacahan region, SE Sivas. *Journal of Faculty of Engineering and Architecture, Çukurova University, Special issue*, 163–177.

Chavez, P. S. (1996). Image-based atmospheric corrections-revisited and improved. *Photogrammetric engineering and remote sensing, 62*(9), 1025-1035.

Çiftçi, Y. (1998). Metalogeny of the ophiolites in the İmranlı–Refahiye area. In *Symposium of Geology and Geophysics of the First 50 Years of the Republic of Turkey* (Abstract, p. 91).

Colman, S. M. (1982). Chemical weathering of basalts and andesites: Evidence from weathering rinds. *Geological Society of America Bulletin, 93*(4), 322–334. https://doi.org/10.3133/pp1246

Crosta, A. P. & Moore, J. M. (1989). Enhancement of Landsat Thematic Mapper imagery for residual soil mapping in SW Minas Gerais State, Brazil: A prospecting case history in greenstone belt terrain. In *9th Thematic Conference on Remote Sensing for Exploration Geology, Calgary, Canada. Ann Arbor (MI): ERIM*, 1173–1187.

Enoh, M. A., Njoku, R. E. & Igbokwe, E. C. (2021). Geospatial interpretation of onshore hydrocarbon micro-seepage induced alterations in soils and sediments by spectral enhancement techniques. *International Journal of Design & Nature and Ecodynamics, 16*(3), 307–313. https://doi.org/10.18280/ijdne.160309

Ercan, T. (1981). *Kula Yöresinin Jeolojisi ve Volkanitlerin Petrolojisi [Geology of Kula Region and Pertology of Volcanics]* [Unpublished Doctoral Dissertation, Phd Thesis]. Istanbul University.

Ercan, T. & Öztunalı, Ö. (1982). Characteristic features and "base surges" bed forms of Kula volcanics. *Türkiye Jeoloji Bülteni (Türkiye Jeoloji Kurumu Bülteni), 25*(2), 117–125. https://jmo.org.tr/resimler/ekler/ec31f2fd081e5a3_ek.pdf

Ercan, T., Günay, E., Dinçel, A., Türkecan, A. ve Küçükayman, A. (1980). *Kula-Selendi Yörelerinin Jeolojisi ve Volkanitlerin Jeolojisi* (Rapor No: 6801). MTA Raporu.

Ercan, T., Fujitani, T. & Matsuda, J-I. (1992). Kula (W. Anatolia) Quaternary volcanism: Petrology and geochemistry. *Geologica Balcanica, 22*(5), 45–56.

Erkan, K. (2015). Geothermal investigations in western Anatolia using equilibrium temperature logs from shallow boreholes. *Solid Earth, 6*, 103–119. https://doi.org/10.5194/se-6-103-2015

Erler, A. & Larson, L. T. (1990). Genetic classification of gold occurrences of the Aegean region of Turkey. In M. Y. Savaşçın & A. H. Eronat (Eds.), *Proceedings of the International Earth Sciences Congress on Aegean Regions (IESCA-1990)* (Vol. 2, pp. 12–23). Dokuz Eylül University.

Genç, Y., Aydın, N. & Tüysüz, N. (1990). Listwaenites related to Narman Hg–Sb mineralization in the eastern Pontides of NE Turkey. In *Proceedings of the International Earth Sciences Congress on Aegean Regions (IESCA-1990)* (Vol. 1, p. 399). Dokuz Eylül University.

Gomboš, M. (2012). The Impact of Clay Minerals on Soil Hydrological Processes. In: Valášková, M. & Martynková, G.S. (Eds.), *Clay Minerals in Nature-Their Characterization, Modification and Application* (pp. 119–147). InTechOpen, Rijeka. https://doi.org/10.5772/47748

Heineke, C., Niedermann, S., Hetzel, R. & Akal, C. (2016). Surface Exposure Dating of Holocene Basalt Flows and Cinder Cones in The Kula Volcanic Field (Western Turkey) Using Cosmogenic ^{3}He and ^{10}Be. *Quaternary Geochronology, 34*, 81-91. https://doi.org/10.1016/j.quageo.2016.04.004

Johnson, K. E. & Koperski, K. (2017). WorldView-3 SWIR land use land cover mineral classification: Cuprite, Nevada. Proceedings of Pecora 20 – Observing a Changing Earth; Science for Decisions Monitoring, Assessment, and Projection (Sioux Falls, SD, 13–16 November 2017). *American Society for Photogrammetry and Remote Sensing* (ASPRS), 7 s.

Jones, H. L. (1929). *Strabo: Geography, Volume VI (Books 13–14)*. Loeb Classical Library 223. Cambridge, MA: Harvard University Press; London: William Heinemann.

Kayadibi, Ö. (2008). Mineral Haritalamada Bant Oranlama ve Crosta Metotları ile Elde Edilen Sonuçların Jeoistatistiksel Olarak Karşılaştırılması. *II. Uzaktan Algılama ve CBS Sempozyumu (UZAL-CBS 2008)*, 13–15 Ekim, Kayseri (Erciyes Üniversitesi).

Khaleghi, M., Ranjbar, H., Abedini, A. & Calagari, A. A. (2020). Synergetic use of the Sentinel-2, ASTER, and Landsat-8 data for hydrothermal alteration and iron oxide minerals mapping in a mine scale. *Acta Geodynamica et Geomaterialia, 17*(2), 311–328. https://doi.org/10.13168/agg.2020.0023

Kılıç, G., Aydoğan, M. S. & Kumral, M. (2018). Preliminary results of the radiolarian-chert hosted manganese deposit within the Vezirler ophiolitic mélange (Kula-Manisa, western Turkey): constraints on the origin, paleo-redox conditions, and depositional environments. *Arabian Journal of Geosciences, 11*(20), Article 628. https://doi.org/10.1007/s12517-018-3984-6

Koç, F. & Kadıoğlu, Y. K. (1996). Mineralogy, geochemistry and precious metal content of Karacakaya (Yunusemre–Eskişehir) listwaenites. *Ofioliti, 21*(2), 125–130.

Larson, L. T., & Erler, A. (1992). Geologic settings and geochemical signatures of twenty-two precious metal prospects in Turkey. In *International Symposium on Eastern Mediterranean Geology* (No. 20, pp. 9–28).

Leo, G. W., Önder, E., Kılıç, M. & Avcı, M. (1978). *Geology and mineral resources of the Kuluncak–Sofular area (Malatya, K-39a1 and K-39a2 quadrangles), Turkey*. (U.S. Geological Survey Bulletin, 1429). U.S. Geological Survey.

Lillesand, T. M., Kiefer, R. W. & Chipman, J. W. (2015). *Remote Sensing and Image Interpretation* (7th ed.). Hoboken, NJ: John Wiley & Sons.

Liu, L., Zhuang, D., Zhou, J. & Qiu, D. (2011). Alteration mineral mapping using masking and Crosta technique for mineral exploration in mid-vegetated areas. *International Journal of Remote Sensing, 32*(7), 1931–1944. https://doi.org/10.1080/01431161003639678

Moix, P., Beccaletto, L., Kozur, H. W., Hochard, C., Rosselet, F. & Stampfli, G. M. (2008). A new classification of the Turkish terranes and sutures and its implication for the paleotectonic history of the region. *Tectonophysics, 451*(1–4), 7–39. https://doi.org/10.1016/j.tecto.2007.11.044

Orynbassarova, E., Ahmadi, H., Adebiyet, B., Bekbotayeva, A., Abdullayeva, T., Beiranvand Pour, A., Ilyassova, A., Serikbayeva, E., Talgarbayeva, D. & Bermukhanova, A. (2025). Mapping alteration minerals associated with Aktogay porphyry copper mineralization in eastern Kazakhstan using Landsat-8 and ASTER satellite sensors. *Minerals, 15*(3), Article 277. https://doi.org/10.3390/min15030277

Oygür, V. & Erler, A. (1999). Intra-plate related carbonatite-hosted bastnaesite-fluorite-barite deposits at the Kızılcaören carbonatite complex, NW Anatolia, Turkey. In *Proceedings of the fifth biennial SGA meeting and the tenth quadrennial IAGOD symposium* (Vol. 1, pp. 225–228).

Reçber, A., Karakaya, N. & Yavuz, F. (1997). Opal occurrences in the listwaenites. In *10th annual meeting of the Mineralogical Society of Turkey* (Abstracts, p. 9).

Rencz, A. N. & Ryerson, R. A. (1999). *Manual of Remote Sensing. Volume 3: Remote sensing for the Earth sciences* (3rd ed.). New York: John Wiley & Sons.

Richardson-Bunbury, J. M. (1996). The Kula volcanic field, western Turkey: The development of a Holocene alkali basalt province and the adjacent normal-faulting graben. *Geological Magazine, 133*(3), 275–283.

Richardson-Bunbury, J. M., Hall, L., Anderson, G. J. & Stannard, A. (2001). The determination of fault movement history from the interaction of local drainage with volcanic episodes. *Geological Magazine, 138*(2), 185–192. https://doi.org/10.1017/S0016756801005271

Segal, D. (1982). Theoretical basis for differentiation of ferric-iron bearing minerals, using Landsat MSS data. In: *Proceedings of the Symposium for remote sensing of environment, 2nd Thematic Conference on Remote Sensing for Exploratory Geology*, Fort Worth, TX (pp. 949-951).

Şen, E. (2002). Kula Bölgesi (*Batı Anadolu, Türkiye) Volkanizmasının Volkanolojik-Petrolojik Gelişiminin İncelenmesi* [Yayımlanmamış Doktora Tezi]. Hacettepe Üniversitesi Fen Bilimleri Enstitüsü Jeoloji Mühendisliği Anabilim Dalı, Ankara.

Şengör, A. M. C., Görür, N. & Şaroğlu, F. (1985). Strike-slip faulting and related basin formation in zones of tectonic escape: Turkey as a case study. In Biddle, K. & Christie-Blick, N. (Eds.), *Strike-slip Deformation, Basin Formation and Sedimentation. Society of Economic Paleontologists and Mineralogists, Special Publication, 37*, 227-264. https://doi.org/10.2110/pec.85.37.0211

Silva, I. M. G., Moura, W. A., Correia, O. & Souza Neto, J.A. (2020). Early evidence of pyrometamorphism and a late hydrothermal alteration related to Albian volcanism in the Pernambuco sedimentary basin, northeast Brazil. *Journal of South American Earth Sciences, 104,* Article 102907. https://doi.org/10.1016/j.jsames.2020.102907

Tangestani, M. H. & Moore, F. (2001). Comparison of three principal component analysis techniques to porphyry copper alteration mapping: A case study, Meiduk area, Kerman, Iran. *Canadian Journal of Remote Sensing, 27*(2), 176–182. https://doi.org/10.1080/07038992.2001.10854931

Tokçaer, M., Agostini, S. & Savaşçın, M. Y. (2005). Geotectonic setting and origin of the youngest Kula volcanics (Western Anatolia), with a new emplacement model. *Turkish Journal of Earth Sciences, 14*(2), 143–166.

Tüysüz, N. & Erler, A. (1993). Geochemistry and evolution of listwaenites in the Kağızman region (Kars, NE Turkey). *Chemie der Erde, 53*, 315–329.

Uçurum, A. (1996). *Geology, geochemistry and mineralization of the silica–carbonate alteration (listwaenite) from Late Cretaceous ophiolitic mélanges at Cürek–Divriği (Sivas Province) and at Güvenç, Karakuz–Hekimhan (Malatya Province), Central East Turkey* [Unpublished doctoral dissertation]. University of Nevada, Reno.

Uçurum, A. (2000). Listwaenites in Turkey: Perspectives on formation and precious metal concentration with reference to occurrences in east-central Anatolia. *Ofioliti, 25*(1), 15–29.

Uçurum, A. & Larson, L. T. (1999). A gold-bearing listwaenite at the Kızıltepe ophiolite, SW Turkey. In *Proceedings of the fifth biennial SGA meeting and the tenth quadrennial IAGOD symposium* (Vol. 2, pp. 841–844).

Üner, T. (2020). Listwaenitization and enrichment of precious metals in the hydrothermal mineralization zones of serpentinites in Sugeçer (Van, Eastern Anatolia, Turkey). *Geochemistry: Exploration, Environment, Analysis, 20*(1), 68–79. https://doi.org/10.1144/geochem2018-087

van der Meer, F. D., van der Werff, H. M. A., van Ruitenbeek, F. J. A., Hecker, C. A., Bakker, W. H., Noomen, M. F., van der Meijde, M., Carranza, E. J. M., de Smeth, J. B. & Woldai, T. (2012). Multi- and hyperspectral geologic remote sensing: A review. *International Journal of Applied Earth Observation and Geoinformation, 14*(1), 112–128. https://doi.org/10.1016/j.jag.2011.08.002

van Gorp, W., Maddy, D., Bridgland, D. R., Demir, T. & Veldkamp, A. (2013). Fluvial response to

Holocene volcanic damming and breaching in the Gediz and Geren rivers, western Turkey. *Geomorphology*, 201, 430-448. https://doi.org/10.1016/j.geomorph.2013.07.016

Yavuz, H., Demir, Y., Kasapçı, C., Uysal, İ. & Helvacı, C. (2022). Geology and genesis of the Silica-Listwaenite hosted Kaymaz gold deposit, Eskişehir, NW-Turkey: Implications from fluid inclusions and pyrite chemistry. *Journal of Asian Earth Sciences: X*, Article 100104. https://doi.org/10.1016/j.jaesx.2022.100104